coatings

MDPI

Article

Water-Borne Photo-Thermal Superhydrophobic Coating for Anti-Icing, Self-Cleaning and Oil–Water Separation

Jinsong Huang, Shengqi Lu, Yan Hu, Liming Liu * and Hui You

School of Mechanical Engineering, Guangxi University, Nanning 530004, China; huangjinsongni@163.com (J.H.); sanchezlu0226@gmail.com (S.L.); yh1832501@163.com (Y.H.); usmlhy@iim.ac.cn (H.Y.)
* Correspondence: llming@gxu.edu.cn

Abstract: Superhydrophobic coatings with photo-thermal effects have advantages in anti-/de-icing and self-cleaning. Here, an eco-friendly and low-cost fabrication of superhydrophobic coating was proposed by spraying a water-borne suspension including carbon black and paraffin wax onto substrate-independent surfaces. The a water-borne suspension coated on stain steel plate showed a strong water-repellence, delaying the ice freezing time to 665 s, which is much higher than that of bare stain steel plate (210 s) under the same experimental condition. The ice-melting time was measured as 120 s under a solar irradiation of 0.1 W/cm^2, while the control group had no sign of ice-melting during the same time. As a concept of proof, the self-cleaning, anti-corrosion, and oil–water separation were enabled by spraying the water-borne suspension on various substrates, demonstrating its diverse performances. Hence, the water-borne superhydrophibic coating provides an efficient, safe, and sustainable solution for wettability-related applications.

Keywords: photo-thermal superhydrophobic coating; anti-icing; self-cleaning; oil–water separation

check for updates

Citation: Huang, J.; Lu, S.; Hu, Y.; Liu, L.; You, H. Water-Borne Photo-Thermal Superhydrophobic Coating for Anti-Icing, Self-Cleaning and Oil–Water Separation. *Coatings* **2024**, *14*, 758. https://doi.org/10.3390/coatings14060758

Academic Editor: Carlo Antonini

Received: 16 May 2024
Revised: 5 June 2024
Accepted: 12 June 2024
Published: 14 June 2024

Copyright: © 2024 by the authors. Licensee MDPI, Basel, Switzerland. This article is an open access article distributed under the terms and conditions of the Creative Commons Attribution (CC BY) license (https://creativecommons.org/licenses/by/4.0/).

1. Introduction

The development of self-cleaning and anti-icing technology has aroused widespread attention in the field of aerospace [1–5] in power transmission cables for the reason that ice accretion can result in the mechanical failure of aircraft with large area paralysis of the power transmission system [6]. Superhydrophobic surfaces with a contact angle (CA_{water}) and rolling angle (RA_{water}) of water above 150° and below 10°, respectively, have an extremely low contact area at the interface adhesion point between solid and liquid and exhibit impressive effects in self-cleaning and anti-/de-icing [7–10]. In addition, superhydrophobic surfaces with photo-thermal effects would further delay icing time and reduce the de-icing force compared with a mono-superhydrophobic surface [11]. Thus, it can be inferred that the combination of active and passive anti-icing technologies is a wise decision to enhance anti-/de-icing performance in cold environments.

Photo-thermal superhydrophobic surface have achieved great attention in the last two decades. A variety of photo-thermal materials such as iron tetraoxide [12], graphene [13–16] and carbon black [17,18] have been selected as the photo-thermal source. Although the reported coatings have a good photothermal de-icing capability, the preparation process is complicated, e.g., Zhang et al. [19] designed a kind of robust durably corrosive superhydrophobic coating with a photothermal effect (DCSCPE) via dual-size Fe_3O_4 nanoparticles to compound the polymers for anti-icing/de-icing performance and chemical resistance properties so as to enhance the versatility of superhydrophobic coatings. Currently, femtosecond lasers can fabricate nanoscale structures with complex geometries and the fabricated nanostructures are utilized to enhance the hydrophobicity of the surface-by-surface energy modification [20]. However, femtosecond laser processing is inefficient and difficult to realize in mass production, e.g., Lin et al. [21] prepared a black coating with resin and CNTs through an air spraying method and used a laser as an etching tool to

peel the pure resin film from the top surface of the coating. Based on this process, they obtained a light-absorbing coating with a porous microstructure. Liu et al. [22] constructed superhydrophobic and optically enhanced absorption graphene arrays on carbon film surfaces via femtosecond laser nanofabrication. Wu et al. [12] reported a Fe_3O_4/fluorinated superhydrophobic epoxy coating. Hence, a facile and low-cost method to fabricate photo-thermal superhydrophobic materials is necessary, which is highly demanded for large-scale production.

Significantly, carbon black has a high light absorption coefficient and ultra-broadband absorption, showing an outstanding solar-responsive capacity [23,24]. However, large amounts of organic solvents are always involved in the hydrophobic modification for the application of self-cleaning and oil–water separation, especially, the fluorides are used as the low surface energy reagents [25,26] which catastrophically damage water and air resources. Hence, solvent-free and nonfluoride fabrication of the superhydrophobic coating to alleviate the environmental burden is highly appealing.

Herein, a superhydrophobic coating with a photo-thermal effect was developed by spraying a water-borne superhydrophobic suspension. The coating is feature of hierarchical micro-nanostructures made up of the accumulated CB particles that are wrapped with the wax with low surface energy, showing a good anti-wettability with CA_{water} of 164° and RA_{water} of 1°, respectively. The self-cleaning effect was verified by releasing water droplets onto the superhydrophobic coating with a tilted angle of 5°. Moreover, anti-/de-icing performance in the aspect of freezing delay time, ice-accretion, ice-adhesion and ice-melting time was evaluated under a solar irradiation of 0.1 W/cm^2. Furthermore, thanks to the selective super-wettability toward water and oil of the coating, a superhydrophobic/superoleophilic mesh was fabricated. The mesh achieved oil–water separation with an oil flux of 9.1×10^4 L/m^2 h and a separation efficiency above 98.5%. The above performance is anticipated to satisfy the eco-friendly and large-scale fabrication of superhydrophobic coatings, which is involved in multifunctional wettability-related applications.

2. Materials and Methods

2.1. Experimental Materials

The metal mesh (100 mesh) and aluminum plates were obtained locally. Anhydrous ethanol (AR, ≥99.7%) and aluminum dihydrogen phosphate (Al $(H_2PO_4)_3$, adhesive) were purchased from Japan Kraton (Kamisu-shi, Japan) D1113BT. Carbon black (CB, AR, ≥99.5%, 20 nm), sodium hydroxide (NaOH, AR, ≥99.7%), sodium chloride (NaCl, AR, ≥99.7%), hydrogen chloride (HCl, AR, ≥99.7%), dichloroethane, methylene chloride, n-hexadecane and kerosene were purchased from Aladdin Industries, Inc. Paraffin, carnauba wax and cetyltrimethyl ammonium bromide (CTAB) were purchased from Aldrich. Sudan III (AR, ≥85%) and methylene blue (AR, ≥85%) were purchased from Aladdin Reagent Ltd. (Shanghai, China).

2.2. Preparation of the Superhydrophobic NPs (SHNPs)

Firstly, the suspension was prepared by dissolving 3 g of the mixed waxes with the same weight ratio of paraffin/carnauba wax and 0.5 g CTAB in 100 mL of boiling ethanol solution. Then, 1 g of CB was added to the suspension, and in order to make the CB disperse into the mixture homogeneously, ultrasonic dispersion was carried out for 5 min. Finally, it was put into a blower purge dryer and dried at 80 °C for 2 h to obtain the SHNPs.

2.3. Preparation of the Photo-Thermal Superhydrophobic Coating (WBSC)

A total of 1 g SHNPs was taken and added to 100 mL of ethanol solution along with 0.02 g of adhesive. In order to make the dispersion more homogeneous, the SHNPs suspension was obtained via ultrasonic dispersion equipment. Then, the appropriate amount of SHNPs suspension was sprayed onto the surface of the aluminum plate with a spray gun at the pressure of 0.6 MPa; it was then placed in a blower purge dryer and dried at 50 °C for 10 min to obtain the photo-thermal superhydrophobic coating (WBSC).

2.4. Oil–Water Separation

For the oil removal mode, the steel mesh was selected as the substrate for separating the immiscible oil–water mixture and SHNPs were sprayed onto a 7 cm^2 steel mesh and placed on the filter. An oil–water mixture of 20 mL of dichloroethane (red) stained with Sudan III and 20 mL of water (blue) stained with methylene blue was poured into the filter device, and due to the superhydrophobic/lipophilic nature of the coatings, the oil could pass through the coatings while the water could not pass through, thus oil–water separation was achieved. The oil flux ($Lm^{-2}h^{-1}$) obtained from the separation can be calculated by the following equation:

$$Flux = V/AT \quad (1)$$

Here, $V(\mathrm{L})$ is the permeate volume, $A(\mathrm{m}^2)$ is the effective filter area of the compressed sample and $T(\mathrm{h})$ is the effective time.

2.5. Measurements of the Hydrophobicity and Anti-Icing Test

The water contact angle (CA) and roll angle (RA) of the WBSC were measured using an optical contact angle meter OCA 20 (Dataphysics, Filderstadt, Germany) at room temperature and ambient pressure by placing a drop of deionized water with a volume of 10 μL on the WBSC and measuring the static contact angle three times at different positions. A 10 μL drop of deionized water was placed on the surface of the WBSC and then the sample stage was rotated until the drop slid off the surface of the WBSC; the tilt angle of the stage was defined as the roll angle.

The contact angle hysteresis (CAH) of the WBSC surface was measured using a contact angle meter. A droplet with an initial volume of 10 μL was placed on the surface of the sample and then the deionized water was added to the droplet at a rate of 0.05 μL/s. The advancing contact angle was measured when the droplet's shape did not change and the contact line began to increase. After the measurement of the advancing contact angle was completed, the liquid was aspirated. When the shape of the droplet did not change during aspiration and the contact line decreased, the receding contact angle was measured. The contact angle hysteresis is calculated by the following equation [27–29]:

$$CAH = ACA - RCA \quad (2)$$

Here, $CAH(^\circ)$ is the contact angle hysteresis, $ACA(^\circ)$ is the advancing contact angle and $RCA(^\circ)$ is the receding contact angle.

In order to investigate the delayed icing time of WBSC in a low-temperature environment, the WBSC samples were placed on a cooling table and the temperature of the cooling table was controlled to -15 ± 3 °C. The relative humidity was set at 25 ± 5% to minimize the effect of ambient condensation on the ice delay test. A syringe was used to drop 10 μL of deionized water onto the surface of the WBSC and a temperature recorder with a measurement accuracy of 0.1 °C was fixed while an industrial camera was used to record the process and time of freezing of the droplets. The time for the droplet to change from a transparent state to an opaque peach-tip state was recorded as the freezing delay time.

A cooling table and a digital force transducer (Aipli SF-100, Pipli, Zhejiang, China) were used as an experimental platform to measure the adhesion strength of ice on the WBSC. We chose the temperature reaching −15 °C as the experimental temperature for ice adhesion strength. After the cooling table was turned on, when the temperature reached −15 °C, a rolling screw-driven force sensor pushed the ice droplets at a speed of 1 mm/s, yielding the maximum peak force. The adhesion strength of ice was obtained by calculating the ratio of the peak force to the contact area of the ice droplet on the substrate. The

accuracy of the digital force sensor was 0.01 N and the median value was taken for five measurements. The ice adhesion strength is calculated via the following equation:

$$\tau_{ice} = F/S \quad (3)$$

Here, $\tau_{ice}(\mathrm{Pa})$ is the ice adhesion strength, $F(\mathrm{N})$ is the measured peak force and $S\left(\mathrm{m}^2\right)$ is the contact area between the ice droplet and the substrate.

To study the photothermal anti-icing and de-icing ability of WBSC, the metal sheet and WBSC samples were placed on the cooling table separately, about 10 µL of deionized water was dripped on the sample surface and the temperature of the cooling table was lowered to -20 ± 3 °C and frozen for 2 h. After the water droplets were completely frozen, the sample surface was irradiated with sunlight simulated by a solar simulator with a light intensity of 1 sun (0.1 W/cm^2). The ice droplets melted on the sample surface while the photothermal ice melting and de-icing process was recorded using an industrial camera. The temperature change of the sample surface was recorded using an intelligent thermal camera.

2.6. Chemical Durability Test

Sandfall was performed to assess the durability of the WBSC under severe abrasion. The surface was impacted at a distance of 20 cm to simulate the hydrophobicity and anti-icing properties of the WBSC over time under sandstorm conditions.

The WBSC were immersed in acidic (1 M HCl), neutral (1 M NaCl) and alkaline (1 M NaOH) solutions, and after 12, 24, 36, 48, 60 and 72 h, the WBSC were removed to test their water contact angles, respectively.

2.7. Water Jet Test

The WBSC surface was fixed under the water outlet at a distance of 20 cm. When carrying out the water jet experiments, the water flow could be controlled by switching the valve and the impact velocity is calculated via the following formula:

$$V_{impact} = K_{\omega}/A_{tap} \quad (4)$$

Here, $V_{impact}(\mathrm{m/s})$ is the impact velocity, $K_{\omega}(\mathrm{L})$ is the volumetric flow and $A_{tap}\left(\mathrm{m}^2\right)$ is the cross-sectional area of the outlet. The entire test was conducted at ambient pressure and temperature (25 °C).

2.8. Characterization

The microscopic morphology of the samples was observed via scanning electron microscopy (SEM, Merlin, Zeiss, Jena, Germany) and the distribution of the elemental composition of the samples was analyzed via energy dispersive spectroscopy (EDS) mapping in SEM. The chemical properties of the samples were characterized using a Fourier Transform Infrared Spectrometer (FTIR, model: WD6901A, manufactured by Tianjin Neng Spectrum Technology Co., Tianjin, China). The contact and roll angles of the sample were tested using a contact angle system OCA 20 (Dataphysics, Germany). The delayed icing time and bouncing process of the droplets were recorded by a high-speed camera (FASTCAM MINI UX100TYPE 200K-M, Photron, Tokyo, Japan). The photothermal de-icing process was filmed and recorded using an industrial camera (ONICK, 200X-2000X, 4 K, Onika Optical, Wuhan, China). An intelligent thermal camera (FOTRIC348+, Inc. 640X480, Houston, TX, USA) was used to measure temperature changes. Sunlight was simulated using a solar simulator (ULTRA-VITALUX, OSRAM, Munich, Germany, 300 W) and light intensity was kept at 1 sun (0.1 W/cm^2) to irradiate the samples.

3. Results and Discussion

3.1. Preparation and Characterization of the Water-Born Superhydrophobic Coating (WBSC)

The water-borne superhydrophobic suspension was prepared via a one-pot heating method; the preparation strategy is schematically illustrated in Figure 1a. The micro-

nanoscale CB and carnauba wax were mixed in a water environment of 70 °C. After the complete dissolution of the carnauba wax, the hydrophobic-modification of CB was achieved since the dissolved wax coated onto the CB, which was verified via the micro-morphology change between the pristine CB and modified CB (Figure 1a). The CB and SHNPs were sprayed onto the metal surface to form a coating and then the contact angle of the coatings was measured separately, which was expressed as the contact angle of CB and SHNPs. Figure 1b shows that the pristine CB was hydrophilic with a CA_{water} of 79.4°, which was far less than the modified CB with a CA_{water} of 163.5°. For the results of measuring the CA using distilled water as a test liquid, the value of the CA_{water} was 157.2° for the V_{drop} = 2 μL, while for V_{drop} = 10 μL, the CA_{water} = 163.5°. The CAH for the surface of MCC was 6.3 ± 0.2°. Such values of CA and CAH indicate the superhydrophobic properties of the formed coatings.

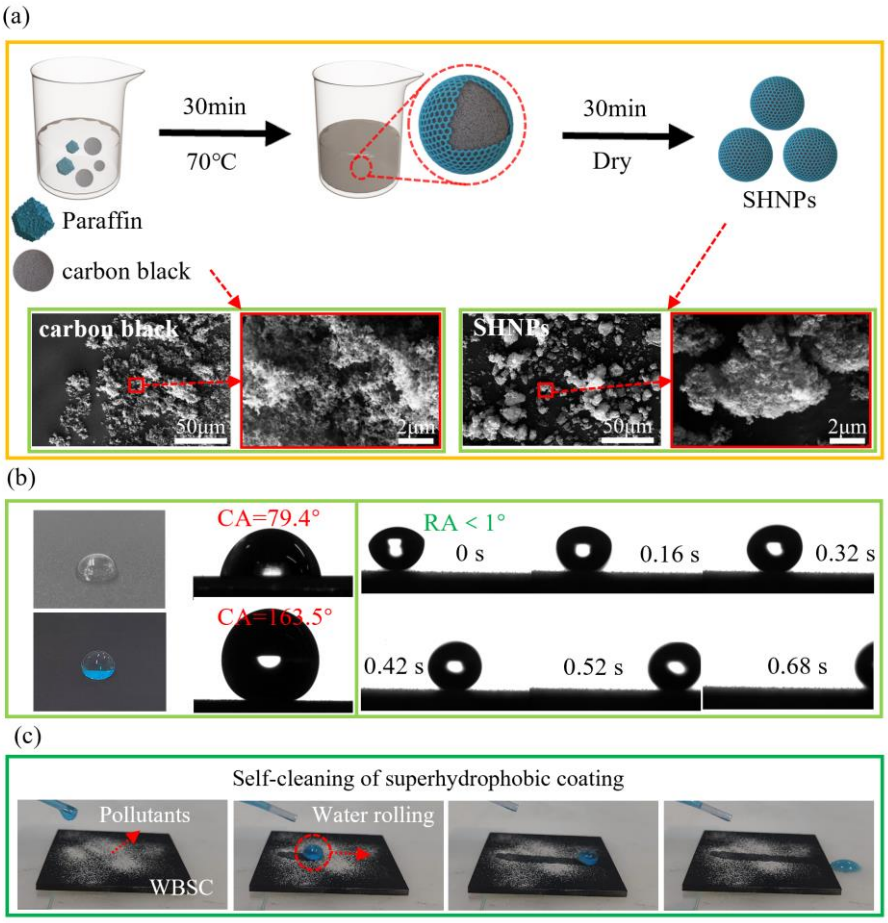


Figure 1. (**a**) Schematic of SHNPs preparation; (**b**) wettability measurement of WBSC; and (**c**) shows the self-cleaning performance of WBSC.

Moreover, in order to enhance the bonding strength between the coating and the substrate, SHNPs were dispersed with an adhesive in an ethanol solution and then sprayed onto a glass surface and exhibited a remarkable self-cleaning effect as shown in Figure 1c. Several water droplets (10–12 μL) dyed with methylene blue fell from a height of 10 cm onto the inclined WBSC covered in a moderate amount of sand. It was clearly observed that sand was detached from the surface following with the rolling water droplet and the clean area showed an excellent stain-resistance performance and self-cleaning effect.

It is acknowledged that surface micronanostructures coupled with low surface energy is the basic rule for the formation of superhydrophobicity. As shown in Figure 2a, SEM micrographs showed that hierarchical microprotrusion was formed on the WBSC and large areas of porosity existed among the gaps of the micronanostructure (high-resolution SEM

images), facilitating the storage of "air-pockets" that isolated the solid–liquid contact. In order to check whether the carnauba wax covered the surface of carbon black uniformly, we carried out the EDS test. Three different sites were selected for EDS analysis and it was found that elemental N was detected in all of them; the average mass fraction of elemental N was 35 wt%. This showed that the carnauba wax covered the surface of the carbon black uniformly and the hydrophilicity of the carbon black itself was replaced, contributing to the superhydrophobicity of the coating. Fourier transform infrared spectroscopy (FTIR) of the CB, the carnauba wax and the WBSC was compared as shown in Figure 2b; the characteristic peaks of -CH_2 and -CH_3 are easily recognized at 2847 cm^{-1} and 2913 cm^{-1}, respectively, which correspond to the functional groups in carnauba wax. Notably, the stretching vibrations of ester group at 1734 cm^{-1} were observed in the FTIR spectra of WBSC, which may be attributed to the hydrogen bonding connection between the -OH groups (3400 cm^{-1}) of CB with the ester groups of the carnauba wax. Then, the methyl groups located in the outer layer provided hydrophobic components for the WBSC [30]. As shown in Figure 2c, the dynamic wettability of the WBSC was characterized by releasing a 10 µL water droplet from a height of 15 cm onto the WBSC surface. It then underwent a contact (0 ms), spread (18 ms) and contraction (21 ms), and then rebounded to a height of 1.98 cm (34 ms). The above analysis illustrates the evolution of micromorphology and chemical composition during the preparation of the water-born superhydrophobic coating.

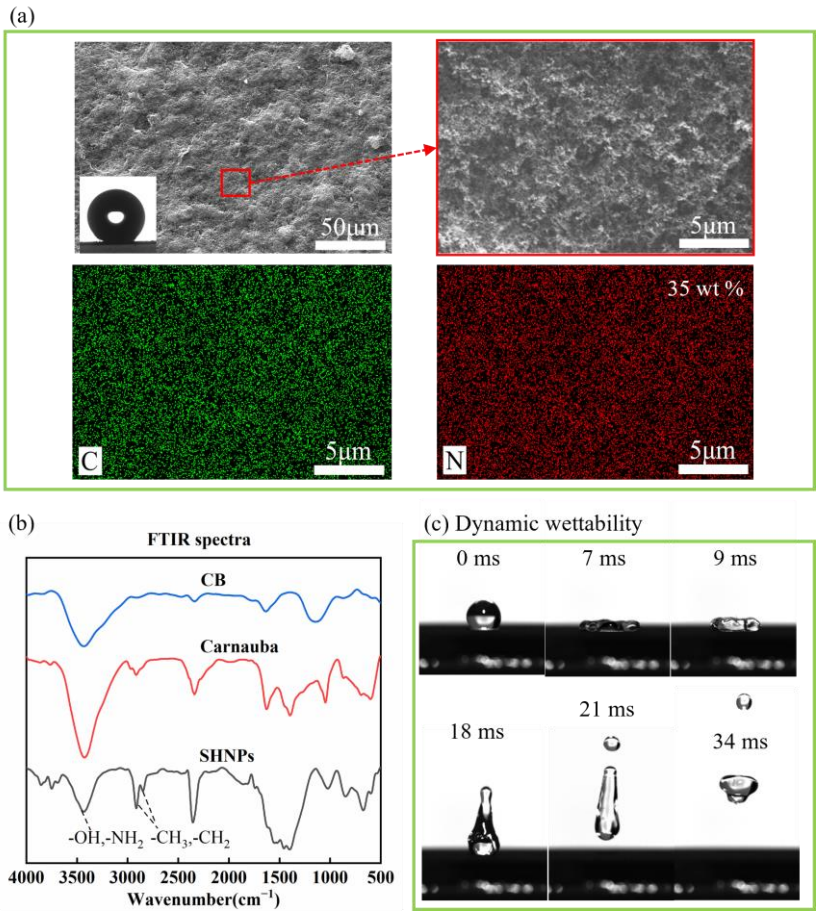


Figure 2. (**a**) SEM image and EDS image of WBSC, the mass fraction of N elements was 35 wt%; (**b**) FTIR spectra of CB, carnauba and SHNPs; and (**c**) the dynamic wettability of the WBSC.

3.2. Mechanical Stability of the WBSC Coating

In the outdoor environment, a superhydrophobic coating faces unpredictable mechanical injuries, e.g., impact from sand or liquid jet. Therefore, we performed impact tests on the WBSC via the free fall of gravel and liquid jets at different speeds. Figure 3

shows that the superhydrophobicity remain intact if the impact speed is below 6.9 m/s (the successive impacting time was 10 min). However, some water stains stuck to the impact area when the jet speed exceeded 18.2 m/s, illustrating that the intrusion pressure of the water jet broke through the Laplace pressure of "air-cushion" that existed in the gaps of the superhydrophobic microstructure. It can be observed that the porosity of the micronanostructure decreased owing to the partial collapse in the impacted area; the mass fraction of N elements decreased to 21 wt% (Figure 4a).

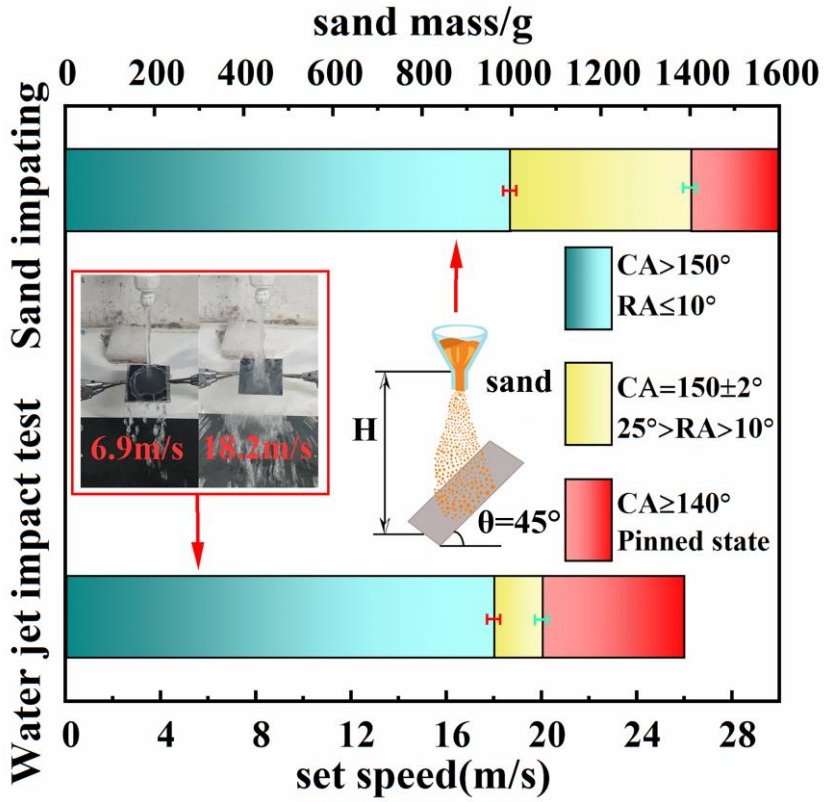


Figure 3. Variation of CA_{water} and RA_{water} at different number of gravel impacts (50 g/cycle, total of 32 cycles) and different water jet impact velocities.

The falling sand impact was further performed to evaluate the mechanical durability of the WBSC coating and the anti-impact ability was quantitatively analyzed via the impact energy equation [31]:

$$W_s = m_s gh = 4/3\pi\rho {R_S}^3 gh \quad (5)$$

Here, ρ is the density of the sand $\rho \approx 2$ g/cm^3, g(m/s^2) is the gravitational acceleration, R_S is the radius of sand $(R_S \approx 200\ \mu m)$. Then, 50 g sand with an impact energy of 0.098j(oule) was released freely from a height of 20 cm to impact onto the WBSC which was recorded as one cycle. As shown in Figure 4b, the variation of CA_{water} and RA_{water} on the WBSC surface was recorded during the successive 32 cycles. As shown in Figure 2c, the CA_{water} decreased from 154° to 152° and the RA_{water} gradually increased from 1° to 8° after the 20 cycles. Moreover, the change of micronanostructure was not obvious, illustrating the good mechanical properties of WBSC against sand impact. After 28 cycles, the CA_{water} was measured as 149.6° as a result of the local detachment of WBSC and the exposure of hydrophilic site.

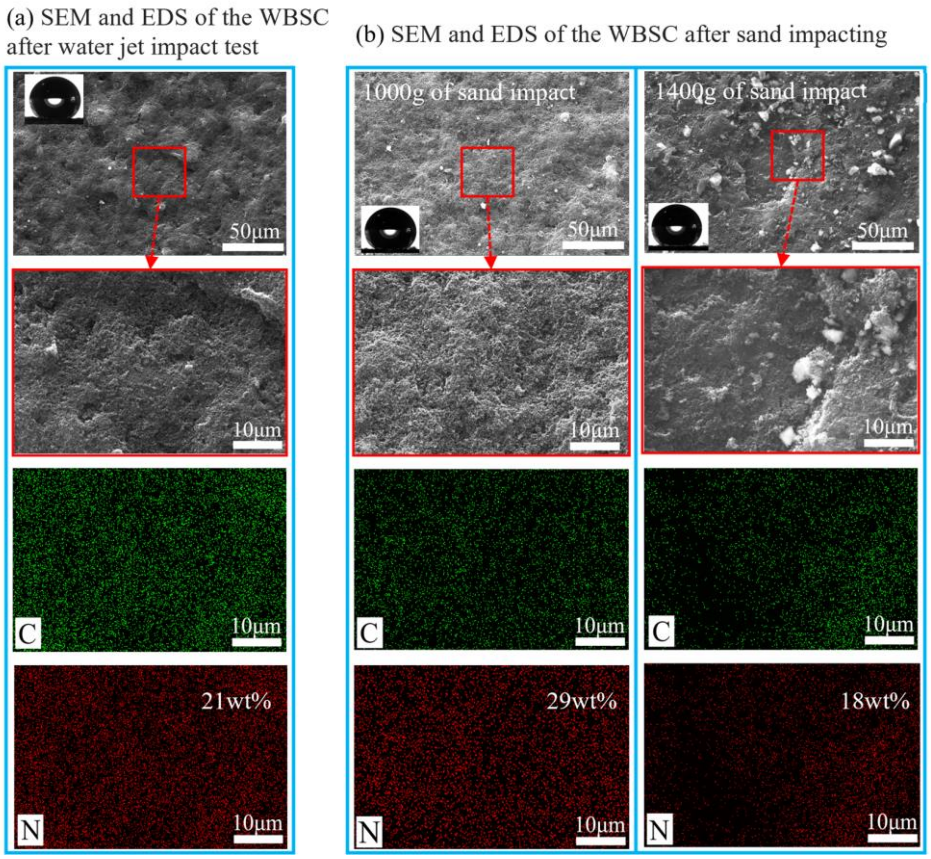


Figure 4. (**a**) SEM micrographs and EDS images of the surface of WBSC after a water jet impact velocity of 18.2 m/s and an impact time of 10 min; (**b**) SEM micrographs and EDS pictures of the surface of WBSC after impact with a different quality of gravel.

The tape-peeling tests were conducted to evaluate the anti-adhesion ability of the WBSC. As shown in Figure 5, the 3M™ VHB™ 5925 tape was used as the adhesion interface and a normal pressure of 200 g was applied to the tape surface for each peel-off cycle. There was little negative influence on the superhydrophobicity and the CA_{water} and RA_{water} were measured as 151° and 5°, respectively, even after the 50 peel-off cycles, demonstrating the good anti-adhesion ability of the WBSC.

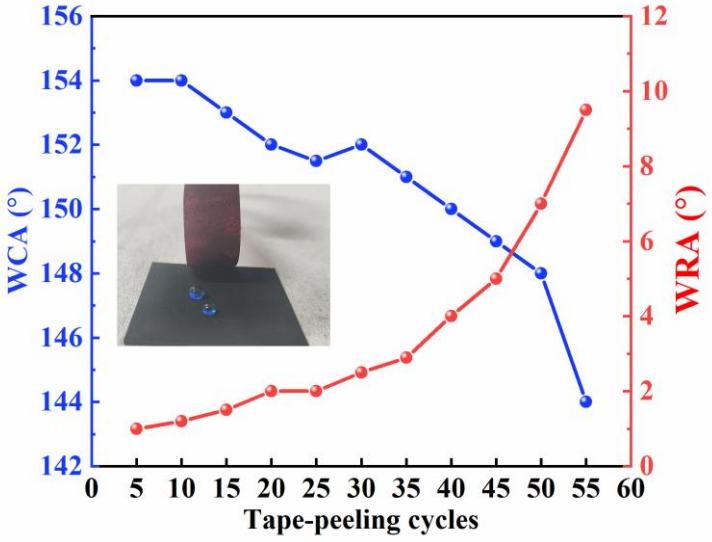


Figure 5. Tape-peeling test and changes of CA_{water} and RA_{water} at different peeling times.

3.3. Anti-/De-Icing Performance and De-Wetting Mechanism

As shown in Figure 6a,b, the icing process, de-icing force and freezing time of the WBSC, stainless steel, PMMA and glass were systemically investigated, respectively. All of the test samples were placed in a homemade freezing device and kept horizontal under the relative humidity of 25%. Then, a 10 μL water droplet was placed on samples as soon as the surface temperature cooled down to −15 ± 0.5 °C. The WBSC exhibited the longest icing delay time of 665 s on average, to compare with that of stainless steel (210 s), PMMA (351 s) and glass (301 s). The control groups showed a faster freezing time compared with the WBSC, which can be attributed to the hydrophilic surface that provides a low nucleation barrier for the ice crystal.

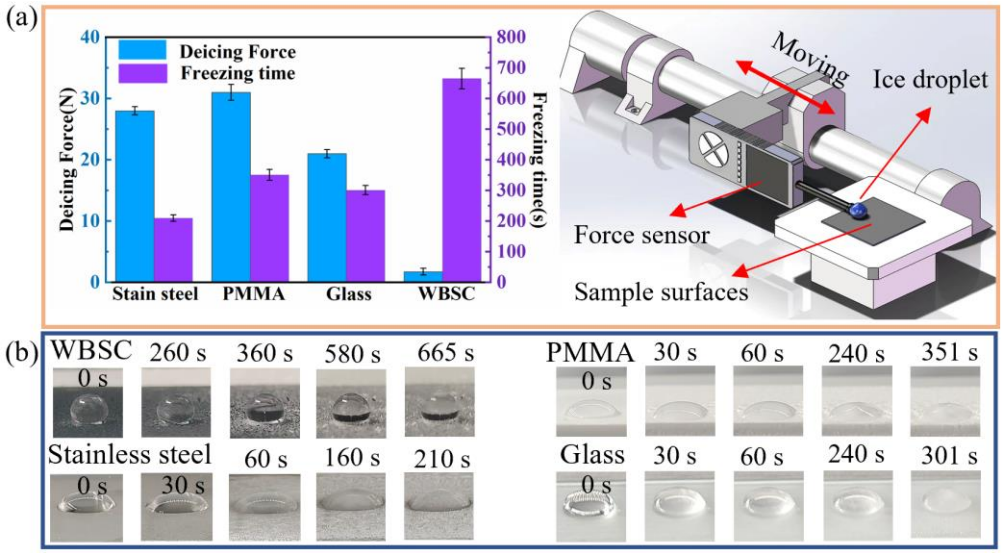


Figure 6. (**a**) Schematic diagrams of icing time and de-icing force, and de-icing force test for metal, PMMA, glass and WBSC surfaces at 25 ± 5% relative humidity. (**b**) Optical photographs of 10 μL droplets iced on different surfaces to form peach tips.

Superhydrophobic surfaces have significant advantages in reducing solid–liquid contact time, delaying freezing time and reducing ice adhesion to the surface. Due to the presence of an "air pocket" at the solid–liquid interface between the superhydrophobic surface and the supercooled droplet, the droplet exhibited a low-adhesion "Cassie" state rather than a high-adhesion "Wenzel" state. The "air pocket" provided strong capillary pressure, causing the droplet to bounce in the opposite direction on the superhydrophobic surface. At the same time, the presence of the "air pocket" reduced the solid–liquid contact area and blocked the heat transfer between the solid–liquid interface, which significantly extended the time for the supercooled droplet to freeze completely. In addition, the smaller contact area also directly led to the reduction in the probability of nucleation and icing of supercooled droplets on the superhydrophobic surface [32]. Thanks to the photo-thermal effect of CB, as shown in Figure 7, the de-icing performance of WBSC was carried out under the solar irradiation of 0.1 W/cm^2. The test samples were entirely frozen on a refrigeration platform with a surface temperature of −15 °C. It is noteworthy that the de-wetting transition from the Wenzel state (frozen) to the Cassie state (melting) was achieved. The thinner ice-frost layer gradually faded away at a faster pace, while the thicker ice droplets (10 μL) melted and slid away from the WBSC at 120 s. The ice-melting process on the WBSC surface was compared with that of the control group at the same time period. The metal surface still remained in its initial frozen state when the frost and ice completely melted on the WBSC surface.

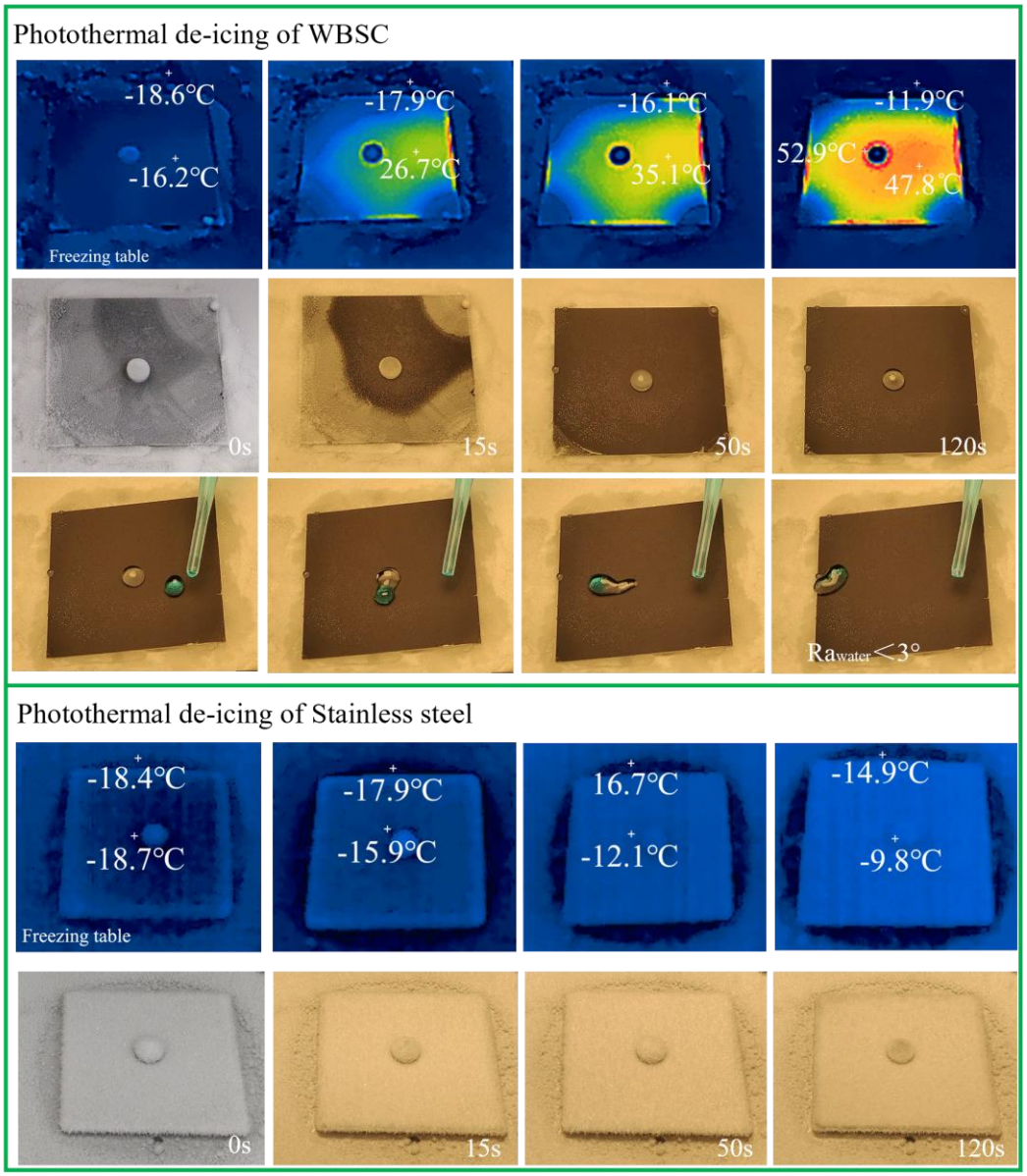


Figure 7. De-icing process of 10 μL droplets on WBSC surface and metal surface.

The variation in surface temperature along with the solar time (1 W/cm^2) was recorded via an infrared thermal imager. Figure 8a shows the surface temperature at room temperature. From 0 to 120 s, the temperature of each surface was uniformly distributed, but the surface of WBSC coating warmed up faster and the highest temperature was higher, up to 81.9 °C.

Moreover, the freezing delay time and de-icing force kept steady during 10 anti-/de-icing tests (Figure 8b). Consequently, the above results illustrate the superiority of the SHNPs in its anti-/de-icing application.

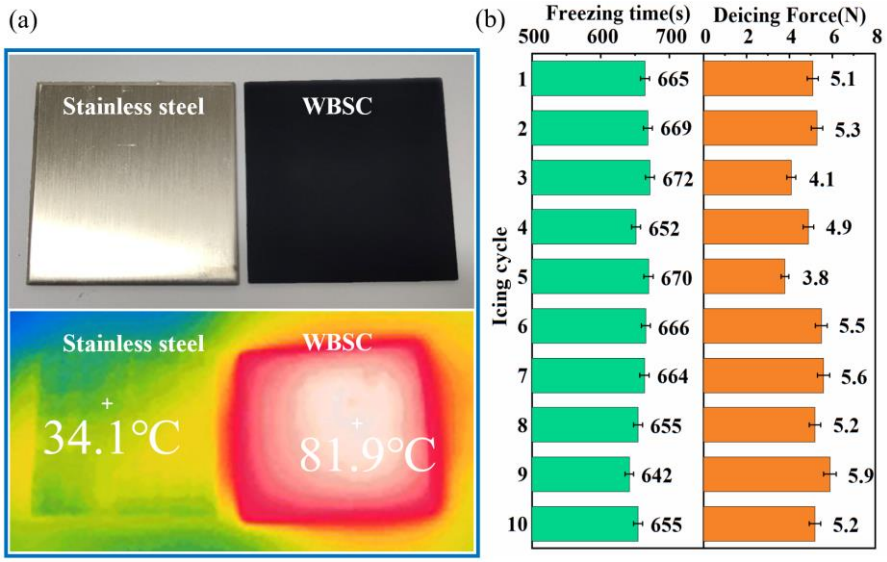


Figure 8. (**a**) Temperature clouds of the pure metal surface and SHNPs surface at room temperature for 120 s with 1 sun of light illumination. The temperatures were 34.1 °C and 81.9 °C, respectively, which show that SHNPs have an excellent photothermal effect. (**b**) Icing time and de-icing power of WBSC surface under 1 sun light illumination, 10 cycles at a temperature of −15 °C.

3.4. Oil–Water Separation Based on the WBSC Coating

A superhydrophobic and superoleophilic porous membrane was prepared by spraying the water-born suspension onto the stainless steel mesh. As shown in Figure 9a, on-demand oil–water separation was enabled by designing a custom-made device. Light or heavy oil–water mixtures were separated in the way of "oil removing", e.g., hexadecane or dichloroethane dyed with Sudan Red III penetrated the mesh and fell into the beaker. While, water colored with methylene blue was blocked on the mesh surface. The separation fluxes were measured as shown in Figure 9b. The flux of oil ranged from 7.5 to 9.1 $Lm^{-2}h^{-1}$, while the flux for kerosene only reached 7.5 $Lm^{-2}h^{-1}$, which may attribute to the high viscosity of kerosene that stuck to the mesh pores. Furthermore, the separation efficiency during the whole oil–water separation process was higher than 98.8%.

The fabricated superhydrophobic coatings were immersed in 1 M HCl, 1 M NaCl and 1 M NaOH solutions, and the corrosion resistance of the coatings was confirmed by measuring the change in the CA_{water} (Figure 9c). As soon as the sample was immersed in the three kinds of solution, a silver mirror-like reflection formed on samples' surfaces which remained completely dry after removal from the solutions. In the neutral solution of 1 M NaCl, the CA_{water} slowly changed from the initial 164°, but always stayed in the superhydrophobic state of >150°; in the strong acid solution of 1 M HCl, the CA_{water} of the sample always stayed in the range of 152° to 165° in the first 50 h; and in the strong alkali solution of 1 M NaOH, the CA_{water} still remained in the superhydrophobic state of >150° for 70 h, indicating that the fabricated superhydrophobic coating was highly resistant to the acidic and alkaline environments. Moreover, the CA_{water} decreased to 150° after 52 h and 72 h immersion in acid and alkali solutions, respectively. The air pockets that existed in the gaps of microstructures that decreased the contact area between the sample and corrosive liquid endowed the WBSC with good anti-corrosion properties. Furthermore, the carnauba wax also had strong chemical inertness in acid and alkali solutions [33].

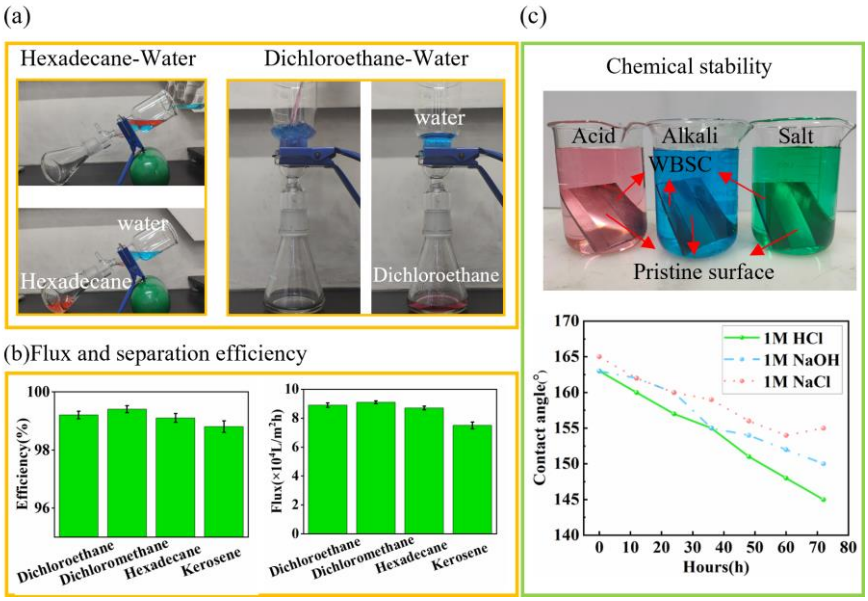


Figure 9. (**a**) Superhydrophobic fabric prepared via WBSC particles with on-demand oil–water separation (**b**) while the separation efficiency and fluxes of dichloroethane, dichloromethane, hexadecane and kerosene were recorded. (**c**) The immersion of WBSC and pristine metal surfaces in a corrosive saturated solution is shown. The CA_{water} of the samples in acid, alkali and salt solutions at fixed time intervals were also recorded, which shows the corrosion resistance of the WBSC.

4. Conclusions

A facile, low-cost and eco-friendly photo-thermal superhydrophobic coating (WBSC) was developed by spraying a water-born suspension. The WBSC exhibited remarkable photo-thermal anti-/de-icing performance, in which the ice freezing time was 665 s and the de-icing strength was 61.8 Kpa under 0.1 W/cm^2 of solar irradiation. Thanks to the flexible preparation strategy, the WBSC can be coated onto various substrates, showing a good self-cleaning effect and oil–water separation. The separation flux and separation efficiency were measured as 9.1 Lm^{-2}h^{-1} and 99.4%, respectively. Moreover, the superhydrophobicity of the WBSC remained intact even after immersion into 1 M HCl (52 h), 1 M NaOH (72 h) and 1 M NaCl (72 h). Furthermore, the mechanical durability of the WBSC was investigated, revealing the good binding strength between coating and substrate during the test of 1500 g of falling sand and a liquid jet propelled at 18.5 m/s. According to these performances of the WBSC, the report is of guiding significance for the large-scale and nonpollution modification strategy of superhydrophobic coatings with a photo-thermal effect.

Author Contributions: Investigation, writing—original draft preparation, data curation, writing—review and editing, J.H.; data curation, writing—review and editing, S.L.; data curation, writing—review and editing, Y.H.; conceptualization, methodology, investigation, writing—review and editing, supervision, L.L.; data curation, writing—review and editing, H.Y. All authors have read and agreed to the published version of the manuscript.

Funding: The work was supported by the Specific Research Project of Guangxi for Research Bases and Talents (AE30100196) and the Natural Science Youth Foundation of Guangxi Province (2023JJB160178).

Institutional Review Board Statement: Not applicable.

Informed Consent Statement: Not applicable.

Data Availability Statement: Data are contained within the article.

Conflicts of Interest: The authors declare no conflict of interest.

References

1. Liu, L.; Wang, H.; Huang, J.; He, M.; Li, S.; Liu, Y.; Li, F.; You, H. One-step fabrication of robust liquid-repellent mesh induced by femtosecond laser. *Chem. Eng. J.* **2023**, *469*, 143853. [CrossRef]
2. Wang, Z.; Peng, S.; Wu, L.; Weng, Z. Construction of ultra-long service life self-cleaning slippery surface on superhydrophobicity functionalized by ATRP treatment. *Chem. Eng. J.* **2022**, *428*, 130997. [CrossRef]
3. Wang, Z.; Zhao, Z.; Wen, G.; Zhu, Y.; Chen, J.; Jing, X.; Sun, S.; Zhang, L.; Liu, X.; Chen, H. Fracture-Promoted Ultraslippery Ice Detachment Interface for Long-Lasting Anti-icing. *ACS Nano* **2023**, *17*, 13724–13733. [CrossRef] [PubMed]
4. Li, J.; Wei, Y.; Huang, Z.; Wang, F.; Yan, X.; Wu, Z. Electrohydrodynamic behavior of water droplets on a horizontal super hydrophobic surface and its self-cleaning application. *Appl. Surf. Sci.* **2017**, *403*, 133–140. [CrossRef]
5. Lin, Y.; Chen, H.; Wang, G.; Liu, A. Recent Progress in Preparation and Anti-Icing Applications of Superhydrophobic Coatings. *Coatings* **2018**, *8*, 208. [CrossRef]
6. Zhou, M.; Zhang, L.; Zhong, L.; Chen, M.; Zhu, L.; Zhang, T.; Han, X.; Hou, Y.; Zheng, Y. Robust Photothermal Icephobic Surface with Mechanical Durability of Multi-Bioinspired Structures. *Adv. Mater.* **2024**, *36*, 2305322. [CrossRef]
7. Chen, G.; Xu, Y.; Zhang, B.; Zhou, Y.; Wang, S.; Meng, Y.; Huang, L.; Song, J. Superhydrophobic coating with super-high adhesive strength to substrate. *Mater. Lett.* **2023**, *351*, 135084. [CrossRef]
8. Han, S.; Yao, T.; Yang, X. Preparation and anti-icing properties of a hydrophobic emulsified asphalt coating. *Constr. Build. Mater.* **2019**, *220*, 214–227. [CrossRef]
9. Yu, Y.; Chen, S.; Jia, Y.; Qi, T.; Xiao, L.; Cui, X.; Zhuang, D.; Wei, J. Ultra-black and self-cleaning all carbon nanotube hybrid films for efficient water desalination and purification. *Carbon* **2020**, *169*, 134–141. [CrossRef]
10. Liu, L.; Chen, S.; Hu, Y.; Pan, W.; Dong, T.; Chen, Y.; Lin, L.; Wang, L. Anti-/Deicing Membranes with Damage Detection and Fast Healing. *Adv. Funct. Mater.* **2024**, 2404760. [CrossRef]
11. Wu, L.; Liu, P.; Hua, X.; Guo, Z.; Liu, W. Photothermal superhydrophobic membrane based on breath figure: Anti-icing and deicing. *Chem. Eng. J.* **2024**, *480*, 147553. [CrossRef]
12. Wu, B.; Cui, X.; Jiang, H.; Wu, N.; Peng, C.; Hu, Z.; Liang, X.; Yan, Y.; Huang, J.; Li, D. A superhydrophobic coating harvesting mechanical robustness, passive anti-icing and active de-icing performances. *J. Colloid Interface Sci.* **2021**, *590*, 301–310. [CrossRef]
13. He, L.; Wang, D.; Ma, T.; Song, J.; Wu, Y.; Li, Y.; Deng, Y.; Zhang, G. Processing and properties of a graphene-reinforced superhydrophobic siloxane. *Mater. Des.* **2023**, *229*, 111856. [CrossRef]
14. Wu, C.; Geng, H.; Tan, S.; Lv, J.; Wang, H.; He, Z.; Wang, J. Highly efficient solar anti-icing/deicing via a hierarchical structured surface. *Mater. Horiz.* **2020**, *7*, 2097–2104. [CrossRef]
15. Zhang, W.; Liu, F.; Li, Y.; Chen, T.; Nwokolo, I.K.; Ahmed, S.; Han, E. Modified Graphene Micropillar Array Superhydrophobic Coating with Strong Anti-Icing Properties and Corrosion Resistance. *Coatings* **2024**, *14*, 247. [CrossRef]
16. Li, S.; Zhong, M.; Zou, Y.; Xu, M.; Liu, X.; Xing, X.; Zhang, H.; Jiang, Y.; Qiu, C.; Qin, W.; et al. Fabrication of Micron-Structured Heatable Graphene Hydrophobic Surfaces for Deicing and Anti-Icing by Laser Direct Writing. *Coatings* **2023**, *13*, 1559. [CrossRef]
17. Dai, Z.; Ding, S.; Lei, M.; Li, S.; Xu, Y.; Zhou, Y.; Zhou, B. A superhydrophobic and anti-corrosion strain sensor for robust underwater applications. *J. Mater. Chem. A Mater. Energy Sustain.* **2021**, *9*, 15282–15293. [CrossRef]
18. Li, X.; Li, X.; Mu, Z.; Li, Y.; Feng, F. An Experimental Study on Biochar/Polypyrrole Coating for Blade Anti-Icing of Wind Turbines. *Coatings* **2023**, *13*, 759. [CrossRef]
19. Zhang, L.; Gao, C.; Zhong, L.; Zhu, L.; Chen, H.; Hou, Y.; Zheng, Y. Robust photothermal superhydrophobic coatings with dual-size micro/nano structure enhance anti-/de-icing and chemical resistance properties. *Chem. Eng. J.* **2022**, *446*, 137461. [CrossRef]
20. Zhou, Z.; Feng, S.; Yang, C.; Ji, C.; Long, Y.; Li, G. Femtosecond laser machining of the novel superhydrophobic microstructure for the oil-water separation. *Surf. Interfaces* **2024**, *45*, 103873. [CrossRef]
21. Lin, Z.; Ma, C.; Ma, Z.; Gao, L.; Chen, W.; Chen, G. Laser etching ultra-black coating with novel anti-icing performance. *Chem. Eng. J.* **2023**, *466*, 143067. [CrossRef]
22. Liu, F.; Gu, Y.; Hu, Y.; Wang, Z.; Ning, Y.; Bradley, R.; Lou, D.; Zhao, B.; Wu, W. Freestanding Ultrathin Precisely Structured Hierarchical Porous Carbon Blackbody Film for Efficient Solar Interfacial Evaporation. *Sol. RRL* **2023**, *7*, 2200803. [CrossRef]
23. Yu, X.; Ye, J.; Li, C.; Yu, Y.; Yang, H.; Wen, L.; Huang, J.; Xu, W.; Wu, Y.; Zhou, Q.; et al. Superhydrophobic, Highly Conductive, and Trilayered Fabric with Connected Carbon Nanotubes for Energy-Efficient Electrical Heating. *ACS Appl. Mater. Interfaces* **2024**, *16*, 26932–26942. [CrossRef] [PubMed]
24. Meng, L.; Park, S. Effect of fluorination of carbon nanotubes on superhydrophobic properties of fluoro-based films. *J. Colloid Interface Sci.* **2010**, *342*, 559–563. [CrossRef] [PubMed]
25. Zhang, J.; Shao, Y.; Hsieh, C.; Chen, Y.; Su, T.; Hsu, J.; Juang, R. Synthesis of magnetic iron oxide nanoparticles onto fluorinated carbon fabrics for contaminant removal and oil-water separation. *Sep. Purif. Technol.* **2017**, *174*, 312–319. [CrossRef]
26. Pan, Y.; Liu, L.; Zhang, Z.; Huang, S.; Hao, Z.; Zhao, X. Surfaces with controllable super-wettability and applications for smart oil-water separation. *Chem. Eng. J.* **2019**, *378*, 122178. [CrossRef]
27. Shi, Z.; Zhang, X. Contact angle hysteresis analysis on superhydrophobic surface based on the design of channel and pillar models. *Mater. Des.* **2017**, *131*, 323–333. [CrossRef]
28. Nadaraia, K.V.; Suchkov, S.N.; Imshinetskiy, I.M.; Mashtalyar, D.V.; Kosianov, D.Y.; Belov, E.A.; Sinebryukhov, S.L.; Gnedenkov, S.V. New superhydrophobic composite coatings on Mg-Mn-Ce magnesium alloy. *J. Magnes. Alloys* **2023**, *11*, 1721–1739. [CrossRef]

29. Huhtamäki, T.; Tian, X.; Korhonen, J.T.; Ras, R.H.A. Surface-wetting characterization using contact-angle measurements. *Nat. Protoc.* **2018**, *13*, 1521–1538. [CrossRef]
30. Wang, D.; Huang, J.; Guo, Z.; Liu, W. Durable mixed edible wax coating with stretching superhydrophobicity. *J. Mater. Chem. A Mater. Energy Sustain.* **2021**, *9*, 1495–1499. [CrossRef]
31. Tan, X.; Wang, Y.; Huang, Z.; Sabin, S.; Xiao, T.; Jiang, L.; Chen, X. Facile Fabrication of a Mechanical, Chemical, Thermal, and Long-Term Outdoor Durable Fluorine-Free Superhydrophobic Coating. *Adv. Mater. Interfaces* **2021**, *8*, 2002209. [CrossRef]
32. Jiang, S.; Diao, Y.; Yang, H. Recent advances of bio-inspired anti-icing surfaces. *Adv. Colloid Interface Sci.* **2022**, *308*, 102756. [CrossRef] [PubMed]
33. Liu, L.; Pan, Y.; Bhushan, B.; Zhao, X. Mechanochemical robust, magnetic-driven, superhydrophobic 3D porous materials for contaminated oil recovery. *J. Colloid Interface Sci.* **2019**, *538*, 25–33. [CrossRef] [PubMed]

Disclaimer/Publisher's Note: The statements, opinions and data contained in all publications are solely those of the individual author(s) and contributor(s) and not of MDPI and/or the editor(s). MDPI and/or the editor(s) disclaim responsibility for any injury to people or property resulting from any ideas, methods, instructions or products referred to in the content.